

# **Peaked bulk crystal nucleation in charged sphere melts from salt concentration dependent crystallization experiments at very low metastability**

J. Schwarz<sup>1</sup>, P. Leiderer<sup>2</sup>, T. Palberg<sup>1\*</sup>

<sup>1</sup>*Institute of Physics, Johannes Gutenberg University, Mainz, Germany*

<sup>2</sup>*Fachbereich Physik, University of Konstanz, Konstanz, Germany*

\*Corresponding author: palberg@uni-mainz.de

Received: 07.07.2021

## **Abstract**

**We determined bulk crystal nucleation rates in aqueous suspensions of charged spheres at low metastability. Experiments were performed in dependence on electrolyte concentration and for two different particle number densities. The time-dependent nucleation rate shows a pronounced initial peak, while post-solidification crystal size distributions are skewed towards larger crystallite sizes. At each concentration, the nucleation rate density initially drops exponentially with increasing salt concentration. The complete data set, however, shows an unexpected scaling of the nucleation rate densities with metastability times the number density of particles. Parameterization of our results in terms of Classical Nucleation Theory reveals unusually low interfacial free energies of the nucleus surfaces and nucleation barriers well below the thermal energy. We tentatively attribute our observations to the presence of doublets introduced by the employed conditioning technique and acting as nucleation seeds.**

## I. INTRODUCTION

Suspensions of colloidal spheres show conveniently accessible length and time scales regarding their structure and dynamics. Therefore, the phase behaviour and crystallization kinetics of these systems have been studied extensively [1, 2, 3, 4, 5, 6]. They are recognized as valuable models for comparison to theory and simulation [7, 8] and for comparison to selected atomic systems like metals [2]. The properties of hard-sphere (HS) like systems are governed by entropy alone and relate to the HS packing fraction [9, 10]. Addition of non-adsorbing polymer introduces so-called depletion attractions with the polymer reservoir packing fraction as second control parameter [11, 12]. For charged spheres (CS, e.g. negatively charged polystyrene particles suspended in water), the metastability of the melt phase can be varied by tuning the effective particle charge, the concentration of screening electrolyte and the number density of particles [13, 14]. With some important exceptions [15, 16, 17], solidification kinetics follows classical models [7, 18, 19]. In these, nucleation is considered as an activated process, followed by growth, which in turn is well described as diffusion-limited (HS) or reaction-controlled (CS) within a Wilson-Frenkel approach [20, 21].

Homogeneous bulk nucleation rate densities,  $J$ , have been determined by light scattering for a large variety of systems at moderate to strong metastability. For HS,  $J$  first increases with increased volume fraction, but then shows a maximum and decreases again [22, 23, 24, 25, 26]. This has been discussed in relation to the HS glass transition and the melt structure at large volume fractions [27]. Locally preferred structures of five-fold symmetry are abundant [28]. These cannot be organized in a space filling manner but may well form the core of larger structures presenting a face centred cubic (fcc) structure on their outside [29]. Despite these issues, experiments and numerical approaches consistently show that parameterization of rate densities by classical nucleation theory (CNT) is feasible at intermediate and large volume fractions, given a reduction in mobility is accounted for [30, 31]. It yields constant reduced interfacial free energies (IFE) of  $\sigma \approx 0.5 k_B T$  per particle in the interface [4]. Homogeneous nucleation in HS has also been studied at lower volume fractions approaching freezing. Here, competing wall nucleation remains negligible and even seeded nucleation remains difficult [32, 33, 34], in particular for small seeds [35]. The latter, however, was demonstrated experimentally e.g. for large spherical seeds or in melts pre-structured by holographic tweezers [36, 37]. By contrast, spontaneous bulk HS nucleation rate densities remain high, and, in fact are several orders of magnitude above the predictions from CNT-based simulations. Various ar-

guments have been discussed to explain this stark deviation, including polydispersity, sedimentation effects, neglect of hydrodynamics in the simulations, or bulk heterogeneous nucleation. However, the discrepancy remains unresolved up to now irrespective of the computational approach chosen [4, 38, 39, 40, 41, 42].

For CS systems, on the other side, parameterization by CNT worked rather well [4, 43, 44]. These systems were so far mostly investigated at large meta-stabilities as a function of particle number density [43, 45, 46, 47, 48]. Again the wealth of studies was devoted to homogeneous bulk nucleation, but also heterogeneous nucleation at the wall was intensively studied [49] and its prevalence at low metastability exploited for growth measurement [50, 51, 52, 53]. A few studies addressed bulk heterogeneous nucleation at added larger and more highly charged spheres or at large structured seeds [54, 55].

Without added seeds, previous bulk studies on CS observed only homogeneous nucleation. Typically, experiments were conducted at fixed particle charge (set by the particle chemistry), deionized conditions (set by thorough deionization in sealed samples or in a conditioning circuit) and variable number density,  $n$  (set by dilution under control by static light scattering) [43]. Particle number densities ranged between 30 and 60  $\mu\text{m}^{-3}$ , yielding steady state nucleation rate densities of  $J = 10^{12} - 10^{17} \text{m}^{-3}\text{s}^{-1}$ , well suited for measurements by time-resolved static light scattering. For lower number densities and rate densities between  $10^9 \text{m}^{-3}\text{s}^{-1} \leq J \leq 10^{12} \text{m}^{-3}\text{s}^{-1}$  post-solidification crystallite size analysis was applied, while for still lower values again time resolved measurements became feasible by video Bragg microscopy [56].

With increasing metastability, homogeneous nucleation rate densities of CS increase exponentially [43]. The increase then slows, but no decrease appears [45]. The equilibrium structure of CS fluids and melts is bcc [57, 58] Also with CS, issues of melt pre-structuring have been discussed [59], e.g. to explain the observed preference for the body centred cubic (bcc) polymorph formation where fcc is the stable crystal phase [60, 61, 62]. Similar to the case of HS, it was observed in simulations that nuclei may show different structures at their core and on their outside surface [63]. Critical nuclei initially show the same body centred structure as the melt, albeit in a more pronounced fashion. Despite these issues, CNT parameterization worked again well for homogeneous nucleation of CS. The slowed increase in  $J$  translates to a linear increase in IFE, showing Turnbull coefficients of about 0.3 similar to those observed in metals [44]. Extrapolating the metastability dependence of the IFE towards the origin gives

values of  $\sigma_0 = 1-2 k_B T$  at freezing. This is of the same order of magnitude as for metal systems. Somewhat counterintuitively, nucleation rates in binary mixtures of CS were observed to be larger than those in the corresponding pure systems [46]. Further, a moderately increased polydispersity appears to lower the IFE and thus favours crystallization in CS [44]. Many systems have been investigated at moderate to large metastability, but only very few at very low metastability [44,64, 65], except for phase behaviour determination [66, 67] and growth experiments [50, 52, 68, 69]. In particular, systematic experimental data on bulk nucleation rate densities are so far missing for low metastability.

The present paper aims at this less well-explored region at low metastability including the fluid-crystal coexistence region. In fact, it originally intended to study homogeneous nucleation rate densities way into the coexistence region and thus provide data parallel to those obtained for HS. This aim, however, required a change in the technical approach.

In the present study we investigate a highly charged polystyrene species (radius 52nm, effective charge  $Z_G = 321e^-$ ) showing a low lying freezing transition in the deionized state at  $n_F = 3.06\mu\text{m}^{-3}$ . We found it difficult to realize a well-controlled way to alter the metastability by varying the number density. We therefore prepared two systems at constant number densities of  $n = 5.4\mu\text{m}^{-3}$  and  $n = 9.5\mu\text{m}^{-3}$  but now varied the concentration of added electrolyte under conductometric control in small steps up to  $0.7\mu\text{molL}^{-1}$ . Using Bragg-video-microscopy as well as post solidification image analysis, we thus could access the salt concentration dependence of nucleation rate densities. Additional growth experiments allowed calibration of the metastability in terms of the chemical potential difference,  $\Delta\mu$ , between melt and crystal as a function of number density and salt concentration. Together this yielded a quantitative characterization of the nucleation kinetics way into the coexistence region and under a finely spaced variation of the metastability. The here observed nucleation kinetics differ considerably from those observed at large meta-stabilities in previous experiments.

We find peaked nucleation rates down to lowest meta-stabilities, and crystallite size distributions are pronouncedly skewed towards larger crystals. For both  $n$ , the observed  $J$  increase exponentially with increasing  $\Delta\mu$ . The complete data set, however, unexpectedly scales with  $n\Delta\mu$ . Moreover, subjecting our data to parameterization by CNT, we extracted very small activation barriers corresponding to extremely small IFEs. Such a behaviour is not expected within CNT under the assumption of homogeneous bulk nucleation starting from a homoge-

neous isotropic and ergodic melt and - *via* one by one particle addition -crossing a barrier arising from the competition between the chemical potential difference and the IFE between such a melt and an ideal bcc crystal.

Checking for possible underlying reasons, we found that due to the special conditioning procedure involved, a non-negligible amount of particle doublets was present in our samples. With this finding we tentatively attribute the peculiar nucleation behaviour of the present system to heterogeneous nucleation at dumbbell shaped seeds. Analysing our data in terms of seeding efficiency reveals an exponential increase of efficiency. This increase starts from very low values at coexistence and approaches unity at large metastability and the larger investigated number density. Such a scenario is not covered by CNT in its extensions to heterogeneous nucleation and therefore calls for alternative theoretical treatments. Our findings may therefore also shed some new light on some of the issues discussed above.

In what follows, we first shortly introduce the materials and methods, then present our results and analysis. In the discussion part, we compare to previous findings, rationalize our findings in terms of bulk heterogeneous nucleation and give a suggestion for the nature of the involved type of nucleation seeds.

## II. SAMPLE CHARACTERIZATION AND CONDITIONING

We investigated commercial Polystyrene latex particles stabilized by  $N = 1200$  strongly acidic surface groups, as determined from titration (PS109\*; Seradyn lot #2011M9R). These particles had been extensively characterized and used as model systems in a variety of previous studies [69, 70, 71, 72, 73, 74, 75]. The *nominal* diameter given by the manufacturer is 109nm. The sample polydispersity is rather small with the ratio of mean and standard deviation of  $s_a/\langle a \rangle = 0.02$ . We found a diameter of  $2a_H = (110.1 \pm 2)$ nm from dynamic light scattering, and  $2a_{AFM} = (106 \pm 15)$ nm from force microscopy on particles deposited on oppositely charged substrates. For our calculations below we used the scattering radius  $a = a_{PQ} = (51 \pm 1)$ nm as obtained from form factor measurements. In suspension, the effective charge numbers are smaller than the group number  $N$ . We determined the number of freely moving protons in the electrostatic double layer from conductivity measurements on deionized samples in dependence on particle number density  $n$  employing Hessinger's model of independent ion migration [76, 77] to be  $Z_\sigma = 459e^-$  (c.f. Fig. A1(a) in Appendix A). This number is close to the expectation from mean field cell-model calculations and used in the determinations of the electrolyte concentration. The interaction strength is calculated using the effective charge

from elasticity measurements on crystallized samples in dependence on  $n$  [78], which amounts to  $Z_G = 321e^-$  (c.f. Fig. A1(b) in Appendix A1).

We employed a closed preparation cycle for sample conditioning, in which the suspension is peristaltically driven through a gas tight tubing system connecting different circuit components. This system allows fast deionization and reproducible adjustment of  $c$  in the  $\mu\text{molar}$  range [79]. It further facilitates integration of several measurements to be performed under identical preparation conditions. Samples are coarsely filtered upon filling the circuit to remove dust and coagulate and other impurities. This also removes a certain amount of particles. The number density therefore can be determined online *via* an integrated static light scattering experiment. A flow-through ion-exchange chamber filled with mixed bed ion exchange resin is used for deionization. The sample conductivity is monitored to equilibrate under continued circling. In the deionised state, residual electrolyte concentrations are dominated by the particle counter-ion contribution and the self-dissociation of water. NaCl solution is then added under by-passing the ion-exchange cell, and conductivity readings are converted to concentrations of added electrolyte,  $c_s$ , again using Hessinger's model with  $n$  and  $Z_\sigma$  as input [76]. Stopping the circulation defined the start of the solidification experiments at  $t = 0$ .

By default the circuit is equipped with a continuous filtering to remove any contaminations like coagulate or resin splinters forming either residual or during cycling. Potential particle loss then necessitates online monitoring of the particle density. This version was employed for the determination of the phase diagram. For the nucleation and growth measurements, we however omitted the filter, to keep the number density strictly constant. We initially regarded contamination as negligible for our experiments. However, after obtaining unexpected results, we addressed this issue explicitly, as unremoved contaminations may potentially act as heterogeneous nucleation seeds. We checked for the presence of contaminations in dependence on conditioning time. We deposited particles on an oppositely charged substrate and subsequently analysed it by scanning force microscopy. This allowed to discriminate PS109\* particles from doublets and other contaminations (technical details are given in Appendix B).

From our analysis, we found doublets to be the majority species of contaminants. We estimate the fraction of doublets to be  $f \leq 10^{-3}$ . This corresponds to upper bounds for the seed number density of  $n_{\text{seed}} \leq 5.4 \cdot 10^{15} \text{m}^{-3}$  and  $n_{\text{seed}} \leq 9.5 \cdot 10^{15} \text{m}^{-3}$  for the two crystallization experiments at lower and higher particle concentration, respectively (see also below in the results section).

In some additional experiments, we checked for the wettability of such seed particles by the crystal phase. Using high resolution microscopy, we observed the distribution of impurities in completely solidified samples. Resin splinters were mainly found at the core of crystallites, larger dust particles and/or larger coagulates were mainly observed at grain boundaries. Doubts, however were observed with only weak preference for either region. Typically, they formed part of the equilibrium crystal structure. This is different to the observations made on smaller charged dopants, which preferably occupy interstitial places [80]. However, in any case, charged impurities smaller than about two times the majority species are integrated into the emerging crystal lattice. In fact, finding them throughout the bulk of colloidal crystals in the present study, demonstrates that this type of seeds is completely wetted by the suspension. This finding is corroborated by the phase behaviour observed in particle mixtures. There an excellent solubility is observed for small amounts of differently sized particles. Only close to the eutectic composition, the miscibility is reduced and the minority species is expelled from the crystal bulk, to form a separate phase [75]. The excellent mixing properties, and thus wettability of odd particles by the crystal phase, is also mirrored in the large value of terminal polydispersity for the crystallization of charged sphere suspensions of  $p_{\text{term}} \approx 13\%$  [81].

### III. RESULTS AND DISCUSSION

#### A. Phase behaviour and growth measurements

The phase diagram of PS109\* is shown in Fig. 1(a). At low  $n$  and large  $c_s$  the suspension is in a fluid state, at larger  $n$  and lower  $c_s$ , samples crystallize in a bcc structure. A coexistence region, which widens with increasing  $n$  and  $c_s$ , is observed between the fluid and crystalline phase. The behaviour is fully consistent with observations on other particle species. As compared to the phase diagram for the less charged twin particle species (PS109; Seradyn lot #2010M9R; [52]), the crystalline region extends to somewhat larger salt concentrations, but otherwise is very similar. Further, the location of the melting line is in good agreement with expectations from simulation [82]. In Fig. 1(a), we further display the range of salt concentration covered in our three kinetic experiments (hatched bars) and the location of the observed freezing points (endpoints of the dashed arrows).

Samples prepared in the meta-stable fluid state readily recrystallize, either via growth after heterogeneous nucleation at the wall of the microscopy cell, or via bulk nucleation followed by growth. Wall crystal growth was measured using Bragg microscopy under external white light illumination in a cell of rectangular cross section ( $10 \times 1 \text{ mm}^2$ , Lightpath Optical, UK)

[52]. In the coexistence region (red hatched bar), recorded velocities slow as a function of time as the extension of the wall crystal approaches its equilibrium value. In this case, we note the initial growth velocities. In the crystal region of the phase diagram at lower salt concentrations, the wall crystal fronts advance linearly in time up to intersection with either the opposing crystal or with bulk nucleated crystals. Here we determine the average velocity by fitting a linear function. Figure 1(b) compares the data for two independent runs and demonstrates excellent reproducibility.

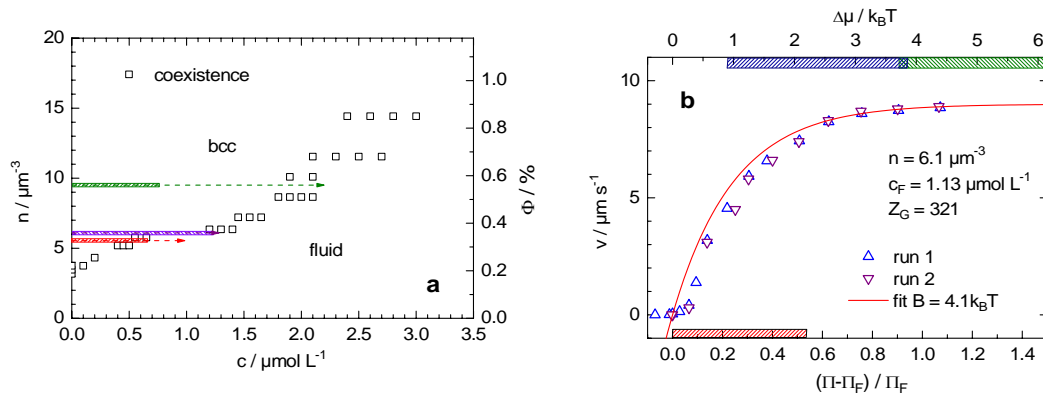


FIG. 1: Phase behaviour and growth measurements. (a) Phase diagram of PS109\* in dependence on concentration of added electrolyte and number density. Open squares denote samples, for which coexisting phases were observed. Arrows and hatched areas denote the experimental  $n$ , the observed freezing points and the range of added electrolyte in the solidification kinetic measurements, respectively. Colours discriminate between the three experiments; red: nucleation experiments at  $n = 5.4\mu\text{m}^{-3}$ ; green: nucleation experiments at  $n = 9.5\mu\text{m}^{-3}$ ; violet: growth experiments at  $n = 6.1\mu\text{m}^{-3}$ . (b) Growth velocities of wall nucleated crystals as a function of the rescaled energy density  $\Pi^*$  as calculated from the experimental parameters and the location of freezing. A WF-growth law fit to the data returns a calibration coefficient of  $B = (4.1 \pm 0.3)k_B T$ . Blue and green hatched bars at the top show the matching ranges of metastability covered in the nucleation experiments at  $n = 5.4\mu\text{m}^{-3}$  and  $n = 9.5\mu\text{m}^{-3}$ , respectively. The red hatched bar indicates the extension of the coexistence region at this number density.

We assessed the metastability of the melt state following the procedure suggested originally by Aastuen [50], and later modified by Würth [52] and Palberg [83]. We exploit the fact that wall crystal growth follows a Wilson-Frenkel (WF) law for reaction-controlled growth in our system:  $v = v_\infty (1 - \exp(-\Delta\mu/k_B T))$ , where  $k_B T$  denotes the thermal energy. To interpret our data,



we assume the chemical potential difference,  $\Delta\mu$  between the melt state and the emerging crystal to be proportional to a reduced energy difference  $\Pi^* = (\Pi - \Pi_F)/\Pi_F$  between the melt and the fluid at freezing (F), i.e.  $\Delta\mu = B\Pi^*$ . Here,  $\Pi = \alpha n V(d_{NN})$  is an energy density calculated from the pair energy of interaction at the nearest neighbour distance,  $V(d_{NN})$ . The pair energy is modelled as screened electrostatic interaction between charged hard spheres (see Appendix A for details, in particular Eqns.(A2) and (A3)). It depends on particle charge and number density as well as on electrolyte concentration.  $d_{NN}$  is the nearest neighbour distance, and  $\alpha$  is an effective coordination number. The parameter  $B$  is then derived from a fit to data obtained in dependence on any of the three control parameters entering  $V(d_{NN})$ . In the present growth experiments,  $n$  and  $Z_G$  are kept constant and only  $c_s$  is varied. Figure 1(b) displays the growth velocities in dependence on  $\Pi^*$  calculated with  $c_F = (1.13 \pm 0.06) \mu\text{molL}^{-1}$ . With increasing metastability, the growth velocity first increases steeply then saturates at a well-defined maximum value of  $v_\infty = 9.0 \mu\text{ms}^{-1}$ .

The figure further shows a least squares fit of a WF-law to the data. The fit describes the data very well. As expected, we find a small systematic deviation across the coexistence region. It is related to the density difference between melt and crystal and increases as freezing is approached. For the present species, this difference, however, remains very small as expected for a low polydispersity system with narrow coexistence region. From the fit, we extract a coefficient  $B = 4.1 \pm 0.3 k_B T$  allowing to calibrate  $\Delta\mu$  (upper scale). Note the slight overlap of the metastability ranges covered by the salt concentration dependent nucleation experiments at  $n = 5.4 \mu\text{m}^{-3}$  and  $n = 9.5 \mu\text{m}^{-3}$  (indicated by the blue and green hatched bars at the top of Fig. 1(b)). This enables the discrimination of the effects of  $n$  and  $c_s$  in the nucleation experiments.

## B. Nucleation experiments

For the bulk nucleation experiments, we used cells with larger depth (5mm) to avoid interference with wall crystal growth. We placed them on the stage of a polarization microscope and observed the sample in transmission between crossed polarizers. This provides a colour contrast between melt and crystals. Only for the latter, the polarization direction of the transmitted light is turned due to dynamical Bragg scattering in dependence on crystal orientation. We used a low magnification objective (5x) to cover a volume  $V_0$  of 5mm radius and 5mm depth. Nucleation rates show a pronounced variation with both salt concentration and particle num-

ber density. At  $n = 5.4\mu\text{m}^{-3}$ , nucleation was slow enough to be directly followed. We performed a direct counting of nucleation events from the recorded videos for time intervals of  $\Delta t = 2.5\text{s}$ . In Fig. 2(a) we display the number of nucleation events as a function of time.

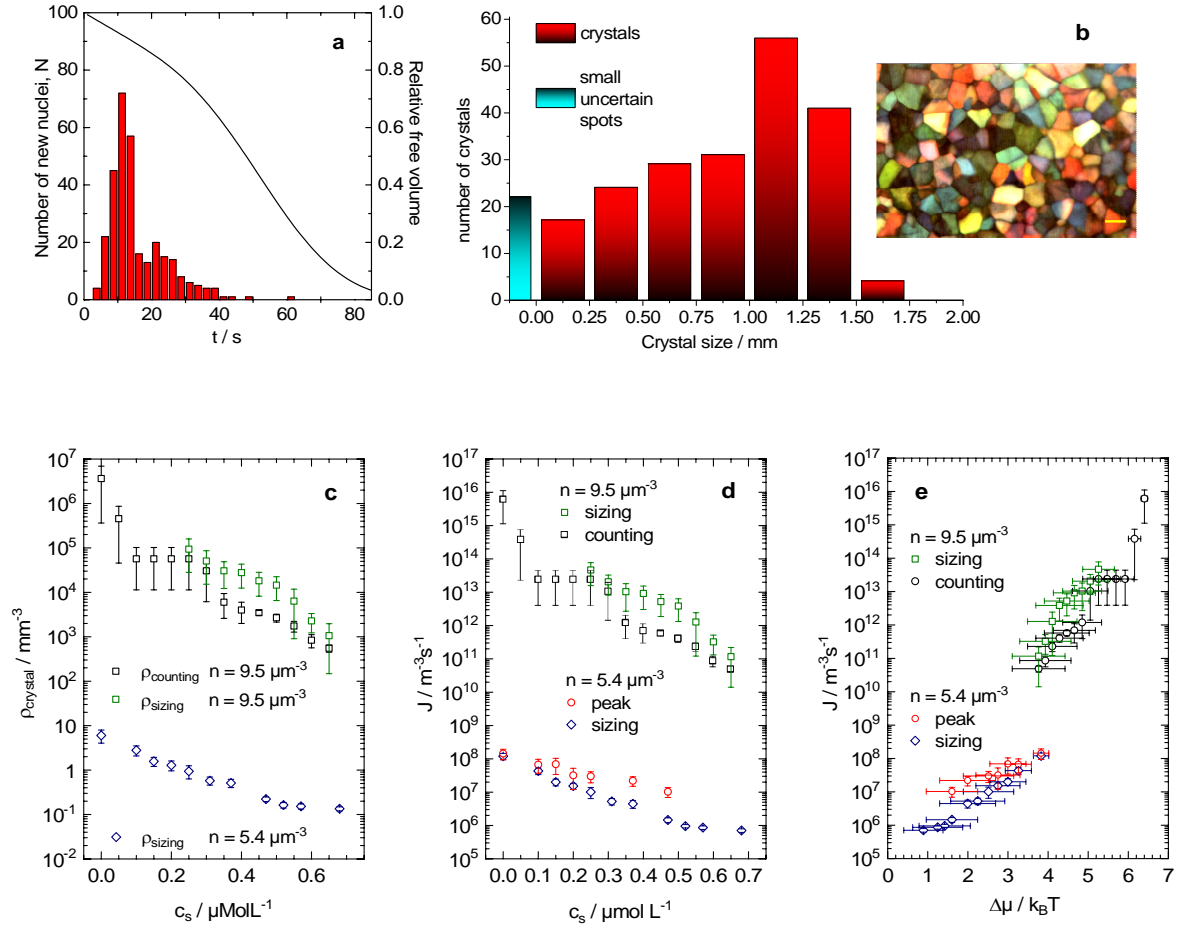


FIG. 2: Nucleation results. (a) Time dependent nucleation rates determined from direct video-microscopic observation. The solid line shows the evolution of the fraction of leftover melt volume (right scale). (b) Crystal size distribution for the post-solidification snapshot shown in the inset. Scale bar  $1000\mu\text{m}$ , image size  $8\times 12\text{mm}^2$ . Small regions with insufficient colour contrast are frequently observed at three crystallite intersections. We here file them under “small uncertain spots”. (c) Crystallite densities as derived from sizing at  $n = 5.4\mu\text{m}^{-3}$  as well as sizing and counting at  $n = 9.5\mu\text{m}^{-3}$  versus concentration of added salt. Vertical error bars denote the combined statistical and systematic uncertainty of  $\rho$ . The error in salt concentration is below symbol size. (d) Nucleation rate densities as a function of concentration of added salt for the two different number densities and evaluation methods as indicated in the key. (e) Nucleation rate densities as a function of metastability for the two different number densities and

evaluation methods as indicated in the key. Here, the horizontal error bars denote the systematic uncertainty arising from the uncertainty in the determination of the freezing salt concentration combining with the uncertainty in actual salt concentration in the calculation of  $\Pi^*$  and the uncertainty of the calibration factor  $B$ .

After a short induction period it steeply rises to a narrow maximum and quickly settles to a very low rate. Figure 2(a) also displays the remaining free volume. The latter was calculated following Wette [56], i.e. using a suitable adaptation of Avrami's theoretical model [84, 85]. It accounts for the volume of newly formed and growing bulk crystals as well as for the wall crystal volume. For the latter quantity we used the known crystal growth velocity in (110) direction at this salt concentration ( $0.1 \mu\text{molL}^{-1}$ ), for the former we used the directionally averaged bulk growth velocity of  $1.05v_{110}$ . The initial linear drop is due to wall crystal growth. The curve steepens as significant bulk crystal growth occurs, and flattens again due to crystallite intersection. Clearly, the nucleation rate drops long before any significant amounts of suspension have solidified. Most importantly, this peaked behaviour did not vanish at larger salt concentrations.

The initial rise in nucleation rate is fast and very short. For salt concentrations up to  $c_s = 0.46 \mu\text{molL}^{-1}$ , however, rates were large enough and statistical scatter low enough to assign a peak nucleation rate density using the percentage of leftover free volume and the observation volume. The peak nucleation rate densities displayed in the semi-logarithmic plots of Fig. 2(d) and e as open red circles show a roughly linear decrease with salt concentration and a roughly linear increase with metastability. In the latter plot, we also show the error bars arising for  $\Delta\mu$ . These are due to the uncertainty of actual salt concentration in the calculation of  $\Pi^*$  and the uncertainty of the calibration factor  $B$  but mostly due to the systematic uncertainty in the exact location of the freezing salt concentration.

We further performed post solidification size analysis [56]. In Fig. 2(b), we illustrate this for the sample at  $c_s = 0.1 \mu\text{molL}^{-1}$  together with a post-solidification snapshot of the analysed sample in the inset. Here, but also at larger salt concentrations, we observe size distributions, which are clearly skewed towards larger crystallite sizes. This skewing direction is fully consistent with our time dependent observations. Moreover, the crystallite edges observed after complete solidification are all straight. According to the model of Johnson and Mehl [86], this is a direct consequence of a nucleation burst at small times. From the obtained sizing data we inferred the average crystallite density  $\rho_c$  and plot it in Fig. 2(c) as a function of salt concentration. Using Avrami-theory, we then infer the effective steady state nucleation rate density  $J$ :

$$J_{AVR}^{ST} = 1.158\nu\rho^{(4/3)} \quad (1)$$

In Fig. 2(c) and (d), we display the obtained rates as blue open diamonds in dependence on salt concentration and metastability, respectively. With increasing  $c_s$ , the rate densities initially decrease in an approximately linear fashion in this semi-logarithmic plot. However, for salt concentrations larger than  $c_s \approx 0.5\mu\text{molL}^{-1}$  the rates level off at a value of  $J \approx 8 \cdot 10^5 \text{m}^{-3}\text{s}^{-1}$ . At low salt concentrations, the rates inferred from sizing meet with the peak nucleation rates. This behaviour is also seen in the dependence on metastability. Note, that for the sizing measurements in dependence on  $\Delta\mu$ , the increase of rate densities with increased metastability accelerates, and at larger metastability, it is steeper than for the peak rate densities.

We now turn to the second series of samples prepared at the larger number density of  $n = 9.5\mu\text{m}^{-3}$ . Here, nucleation was too fast to follow it directly. We therefore resorted to crystallite sizing and crystal counting after complete solidification to determine the average crystallite density  $\rho_c$  and the effective steady state nucleation rate densities. As compared to the sizing at the lower number density, we here faced significantly systematic uncertainties due to the smallness of crystallite sizes. In fact, sizing became possible at all only for salt concentrations larger than  $c_s \geq 2.5\mu\text{molL}^{-1}$ . Further, sizing and counting often yielded significantly different results. The comparison to the data obtained at the lower particle concentration in Fig. 2(c) shows a salt concentration dependent change of  $J$  of several orders of magnitude. Data from both evaluation approaches to  $\rho_c$  overlap reasonably well within the experimental errors. The rate densities now drop from  $J \approx 5 \cdot 10^{15} \text{m}^{-3}\text{s}^{-1}$  in the deionized samples to  $J \approx 10^{11} \text{m}^{-3}\text{s}^{-1}$  at  $c_s = 0.7\mu\text{molL}^{-1}$ . Thus, the qualitative dependence on salt concentration appears to be retained. For each number density the data set shows a roughly linear decrease in  $J$  with increasing salt concentration in this semi-logarithmic plot. When the data are replotted in Fig. 2(d) versus the metastability, we obtain a roughly linear increase of  $J$  with  $\Delta\mu$  for each of the data sets. However, the slope is somewhat steeper at the larger number density. Moreover, at  $\Delta\mu = 4k_B T$ , there is a discontinuity and a jump of about three orders in magnitude to larger  $J$  can be seen at the same metastability. This discontinuous evolution of  $J$  as a function of  $\Delta\mu$  is unexpected.

### C. Data analysis and comparison to previous results

The phenomenological survey above showed differences to previous findings. The discontinuous behaviour of the nucleation rate density as a function of particle number density has not

been seen before in homogeneous bulk nucleation. Further, the observation of peaked bulk nucleation down to very low metastabilities is unusual. In both metals and charged spheres, previous studies showed an extended plateau with steady state nucleation rates framed by a pronounced initial increase and final decrease. For metals, the final decrease is attributed to the release of the heat of fusion resulting in a decrease of metastability [87]. For colloids, it was attributed to a dilution of the melt occurring upon forming the slightly denser crystallites [25]. However, for both metals and charged colloids, the extension of the plateau was found to shrink with increasing metastability, leading to a peaked nucleation only at large metastability [2, 56, 59]. Then, the non-steady nucleation could be successfully interpreted as quickly terminating burst, and a corresponding steady state nucleation rate density could be estimated [2, 93]. By contrast, the here observed behaviour extends way into the coexistence region, while the initial rise covers too few points to assign a steady state nucleation rate  $J^{ST}$  from its initial slope.

To quantify these observations further and to compare to previous findings obtained at moderate to large metastability, we next parameterize our results within classical nucleation theory (CNT) for homogeneous bulk nucleation. CNT was originally developed as macroscopic theory to describe the condensation of droplets and later adapted to describe also crystallization. [88, 89, 90, 91, 92, 93]. We are aware of the many assumptions made within and the controversial discussion of this approach. Still, it successfully captures the crystallization kinetics of some systems including simple metals [94] and charged colloidal spheres [4]. It then allows deriving estimates for the key parameters of homogeneous nucleation [44]. In essence, CNT views homogeneous nucleation as an activated process involving one-by-one particle addition. An energy barrier separates the initial homogeneous, isotropic melt (thought to share the structural properties of an equilibrium fluid) and the final perfect crystal phase. It emerges from the competition between the free energy gain obtained in forming the crystal and free energy needed to create the sharp interface of a spherical cluster:  $\Delta G = (4\pi/3)r^3 n\Delta\mu + 4\pi r^2\gamma$ , where  $\gamma$  is the interfacial free energy. Further, all structural details of the interface and the involved phases are ignored. Under these boundary conditions, the steady state CNT homogeneous nucleation rate reads:

$$J^{ST} = k^+(n^*)ZN_{eq}(n^*) = J_0 \exp\left(-\frac{\Delta G^*}{k_B T}\right) = J_0 \exp\left(-\frac{16\pi}{3} \frac{\gamma^3}{(n\Delta\mu)^2 k_B T}\right) \quad (3),$$

where  $n^*$  is the number of particles in the critical cluster,  $k^+(n^*)$  is the attachment rate to the critical cluster,  $Z = (|\Delta\mu| / 6k_B T n^*)$  is the Zeldovich factor accounting for the shape and width of the barrier [7, 89, 90, 95].  $N_{eq}(n^*)$  is the equilibrium number of critical clusters replaced in

the second step by the Boltzmann term involving the barrier height  $\Delta G^*$ .  $k^+(n^*)$  and  $Z$  are combined to give the kinetic pre-factor  $J_0$  characterizing the maximum possible steady state nucleation rate density.

For colloid crystal nucleation from the melt,  $J_0$  depends only weakly on  $n$  and  $\gamma$  [43]. It scales with the long-time self-diffusion coefficient [9], which is approximated via the dynamic freezing criterion [72, 73, 96]. Neglecting the small dependence on  $\gamma$  of the pre-factor,  $\gamma$  is then obtained as the cube root of the  $\Delta\mu$ -dependent slope from a plot of the natural logarithm of  $J$  versus  $1/(n\Delta\mu)^2$ . We illustrate this approach in Fig. 3(a). The main part of the figure shows all data and their dependence on  $1/(n\Delta\mu)^2$ . The inset exemplarily displays the 3 point and 4 point linear fits to the data obtained from sizing at  $n = 5.4\mu\text{m}^{-3}$  (Plots for the other data sets and additional material can be found in Appendix D, Figs. A3, A4 and A5). We normalize  $\gamma$  by the area taken by a particle in the nucleus surface and express it in units of thermal energy:  $\sigma = \gamma d_{\text{NN}}^2 / k_{\text{B}}T$ . Results for reduced interfacial free energy of the sample at  $n = 5.4\mu\text{m}^{-3}$  are displayed in Fig. 3(b). The vertical error bars here derive from the standard errors of the fits in Fig. 3(a) at a confidence level of 0.95. At  $\Delta\mu = 3k_{\text{B}}T$ ,  $\gamma = 4.5\text{Jm}^{-2}$ , respectively  $\sigma = 0.25k_{\text{B}}T$ . Both data sets overlap within the fitting errors, and  $\sigma$  decreases roughly linearly with decreasing  $\Delta\mu$ . However, it approaches zero close to  $\Delta\mu \approx 1k_{\text{B}}T$ . The solid lines are fits of  $\sigma = \sigma_0 + C_{\text{T}}\Delta\mu$  to the data returning a Turnbull coefficient of  $C_{\text{T}} = (0.092 \pm 0.004)\Delta\mu$  ( $(0.084 \pm 0.017)\Delta\mu$ ) for the data from sizing (peak height).

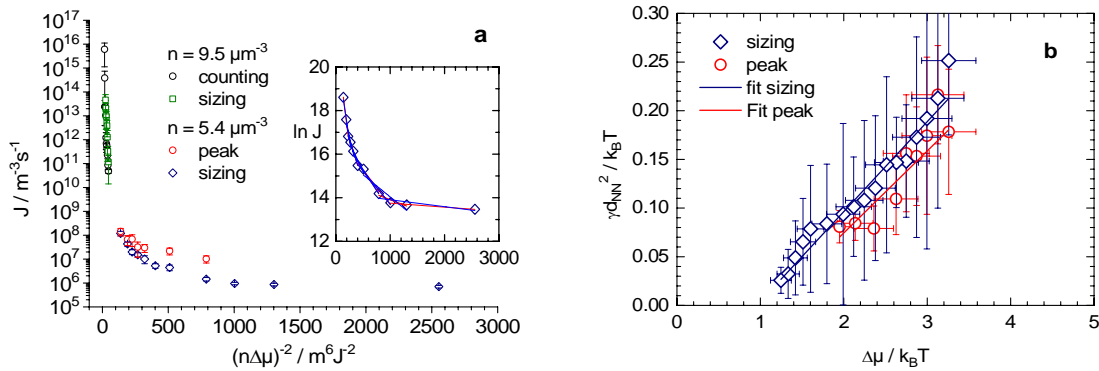


FIG. 3: CNT parameterization. Symbols as before and as indicated in the key. (a) Nucleation rate densities plotted versus  $1/(n\Delta\mu)^2$ . Inset: natural logarithm of  $J$  plotted versus  $1/(n\Delta\mu)^2$  for the sizing data obtained at  $n = 5.4\mu\text{m}^{-3}$ . Solid lines are least squares fits through three (red) and four (blue) points. (b) Reduced IFE in units of the thermal energy as obtained from the

fits versus metastability for the data taken at  $n = 5.4\mu\text{m}^{-3}$ . Solid lines are least squares linear fits returning the slope  $m = C_T$ .

Such a behaviour is at variance to previous findings on charged spheres. In Fig. 4(a), we compare it to two other systems, PnBAPS70 [54, 65, 97] and PnBAPS68 [43] both investigated in dependence on number density. There, the reduced IFE is much larger and extrapolates to a finite  $\sigma_0$  at zero  $\Delta\mu$ . The here obtained values for  $\sigma$  are even significantly smaller than the IFE of hard spheres (dashed line) and extrapolate to negative  $\sigma$ . Further, a Turnbull coefficient of  $C_T \approx 0.1$  is much lower than the value of 0.3 observed before, which is in good agreement with that found for bcc crystallizing metals [Hoyt]. In Fig. 4(b) we plot the critical radii calculated as  $r_{\text{crit}} = 2\gamma/n\Delta\mu$ . For PS109\* this parameter increases with metastability, whereas for PnBAPS68 and PnBAPS70 it follows the CNT expectation for homogeneous bulk nucleation showing a decrease with  $\Delta\mu$ . Figure 4(c) shows curves of the free energy as a function of the nucleus radius  $r$  as calculated using  $\Delta G(r) = -(4\pi/3)r^3 n\Delta\mu + 4\pi r^2 \gamma$ . For deionised PnBAPS68 at  $n = 60.9\mu\text{m}^{-3}$ ,  $\Delta\mu \approx 9.9k_B T$  and  $\gamma \approx 65k_B T\mu\text{m}^{-2}$  the initial rise is well pronounced. A maximum value of  $\Delta G^* \approx 12.7k_B T$  is reached at  $r_{\text{crit}} = 0.22\mu\text{m}$ . Barriers at lower  $\Delta\mu$  are even much larger for PNBAPS68. By contrast, for PS109\* the curves are much shallower and maxima are all well below  $1k_B T$ . In fact, they appear to vanish as the salt concentration is increased.

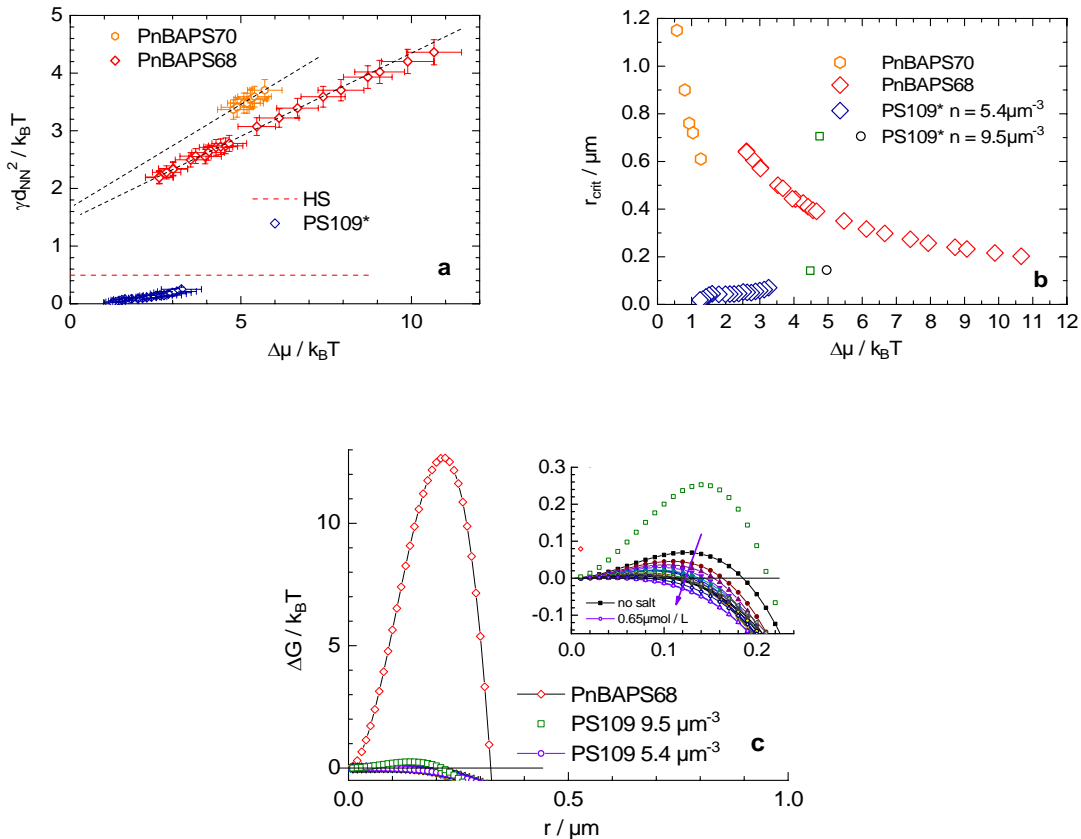


FIG. 4: Comparison of CNT parameters to those obtained for other charged sphere species. (a) Reduced IFE in dependence on  $\Delta\mu$ . Data for PS109\* taken at  $n = 5.4\mu\text{m}^{-3}$  are compared to two data sets from previous measurements, in which good agreement with the CNT expectations for homogeneous bulk nucleation was observed: PnBAPS68 [43] and PnBAPS70 [97]. Both latter systems show much larger reduced IFE, which, moreover extrapolate to a reduced equilibrium IFE of  $1.5k_{\text{B}}T$  and  $1.7k_{\text{B}}T$ . We also display the IFE of HS systems [23] which amounts to  $0.51k_{\text{B}}T$  (dashed red line). (b) Critical radii in dependence on  $\Delta\mu$ . PnBAPS68 [43] and PnBPAPS70 [65, 97] illustrate the behaviour expected from CNT for homogeneous bulk nucleation as seen in many previous systems before:  $r_{\text{crit}}$  decreases with  $\Delta\mu$ . For PS109\*,  $r_{\text{crit}}$  increases with  $\Delta\mu$ . (c) Nucleus free energies  $\Delta G$  in dependence on nucleus radius as calculated from the obtained CNT parameters. Symbols denote: red squares: deionized PnBAPS68 at  $60.9\mu\text{m}^{-3}$ ; open green squares: PS109\* at  $9.5\mu\text{m}^{-3}$ ; open violet circles: PS109\* at  $5.4\mu\text{m}^{-3}$  and  $c_s = 0.65\mu\text{molL}^{-1}$ . The inset shows a magnification of the free energy curves of PS109\* at  $5.4\mu\text{m}^{-3}$  with the salt concentration increasing from zero (black solid squares, upper curve at  $5.4\mu\text{m}^{-3}$ ) to  $c_s = 0.65\mu\text{molL}^{-1}$  (open violet squares, lowest curve). The arrow denotes increasing salt concentration. Note the low maximum values for PS109\* irrespective of sample parameters and the tendency to decrease further with increasing salt concentration.

To summarize our observations for PS109\*, we investigated a fully inconspicuous, highly charged system of comparably low polydispersity in the region of low melt metastability including parts of the coexistence region. Bulk nucleation rates determined from different approaches vary for increased salt concentrations from  $J = 10^{16}\text{m}^{-3}\text{s}^{-1}$  to  $J = 10^{11}\text{m}^{-3}\text{s}^{-1}$  at  $n = 9.5\mu\text{m}^{-3}$  and from  $J = 10^8\text{m}^{-3}\text{s}^{-1}$  to  $J = 10^6\text{m}^{-3}\text{s}^{-1}$  at  $n = 5.4\mu\text{m}^{-3}$ . We observe peaked nucleation of bulk crystals and a crystallite size distribution skewed towards larger crystals way into the coexistence region. Parameterization along the lines of CNT yielded quantitative and qualitative deviations from previous experiments as well as from the CNT expectations. In fact, according to this parameterization, the nucleation events in our experiments appear to be practically barrierless. We conclude that crystallization in PS109\* does not follow the standard path for bulk homogeneous nucleation.

#### D. Heterogeneous nucleation at doublets

The deviations from previous work and from the CNT expectations together with the finding of candidate seed particles suggests that we encountered heterogeneous nucleation at particle doublets. Heterogeneous nucleation is very common in natural systems and deliberately used



in a large variety of industrial processes ranging from the growth of single crystals over snow production to grain refinement [7]. It also is theoretically more demanding. Within CNT, modelling is possible for the transition from non-wetting to completely wetting seeds exhibiting some simple geometry (c.f. Appendix C). This was successfully exploited in the investigation of charged sphere nucleation at flat substrates [65]. At low metastability, heterogeneous nucleation was found to be an activated process involving nuclei of spherical cap morphology. With increasing metastability the contact angle vanished and at crystallization directly proceeded by growth from a pre-ordered layer [49, 65]. Above the transition, however, one of the key assumptions of CNT is lost. Namely: with a vanished nucleation barrier, heterogeneous nucleation is no longer an activated process. The same is expected to apply for the present case, where the doublets are completely wetted by the melt, as evidenced by their homogeneous distribution throughout the formed crystals.

A useful parameter for the characterization of heterogeneous nucleation is the so-called seeding efficiency  $\eta = \rho / n_{\text{seed}}$  given as the ratio of past solidification crystallite density to seed density. In colloidal systems with added large, completely wetting seeds, it was observed to be very close to unity [54]. In the present work, the seed density is estimated as upper bound from the upper bound for the doublet fraction  $f_D \leq 10^{-3}$  assumed to be identical for both experiments. In the present experiments, all efficiencies are below unity. Plotting  $\eta$  as a function of  $\Delta\mu$ , results in two data groups for the two densities, each increasing exponentially with  $\Delta\mu$  and a three orders of magnitude discontinuity upon going from the lower to the larger density at same meta-stability (c.f. Fig. A5 in Appendix D). However, when plotting  $\eta$  in dependence on  $n_{\text{seed}}\Delta\mu$ , all seeding efficiencies arrange on a single curve. Figure 5(b) shows that  $\eta$  increases exponentially with the product of metastability and seed concentration for both experiments.

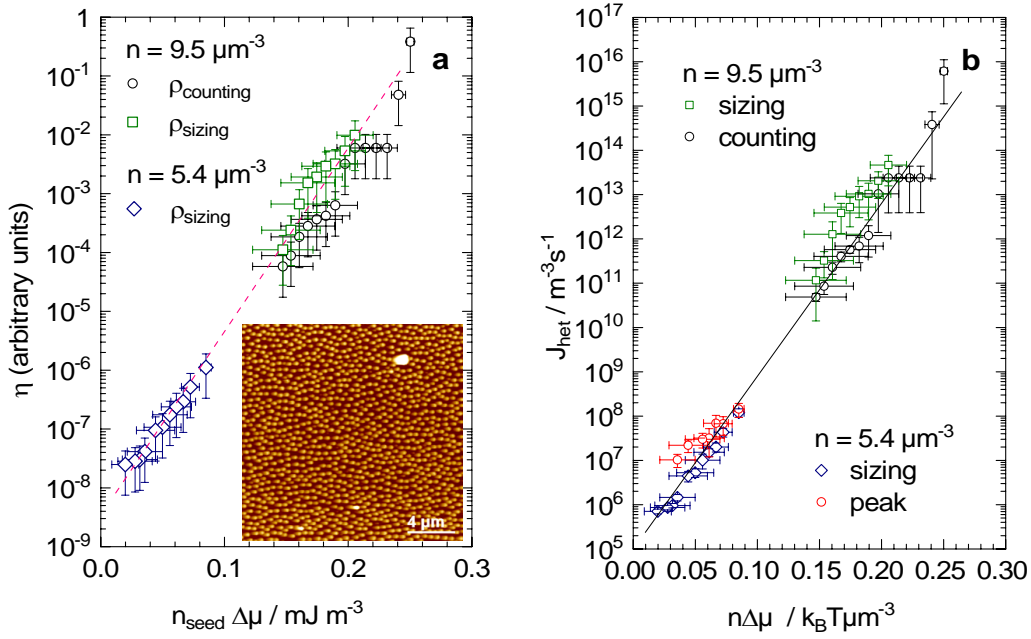


FIG. 5: Heterogeneous nucleation (a) Efficiency of heterogeneous nucleation as a function of  $n$  times the reduced energy density  $\Pi^*$  assuming constant seed fraction for both experiments. Inset: AFM image of particles and impurities deposited on Polyvinylpyridine-coated glass slides by dip coating as used for composition analysis of PS109\*. This image was selected for showing both seed candidate types: two particle doublets (white spots at the bottom) and ion exchange resin debris (large white spot at top right). (b) Data of Fig. 2(d) replotted as a function of  $n\Delta\mu$ . The heterogeneous nucleation rate densities,  $J_{\text{het}}$  arrange on a straight line indicating an exponential dependence of  $J_{\text{het}}$  on  $n\Delta\mu$ . Note that for the present experiments all  $\eta$  stay well below unity.

The seeding efficiency depends on the wettability of the seeds by the mother and daughter phase as well as on seed size and shape. It further is thought to depend on the matching of structure between the nucleating surface or seed and the adjacent phases. The different findings in Engelbrecht's and our work are therefore understood as reflecting the different experimental boundary conditions. The previous study [54] was conducted at large number densities ( $n \approx 25\mu\text{m}^{-3} \gg n_f$ ) providing large nucleation rates and zero density difference between melt and solid as well as small seed densities resulting in  $f_{\text{seed}} = 10^{-11} - 10^{-7}$ . For increasing seed concentrations under otherwise constant conditions, the authors reported a superseding of homogeneous nucleation by heterogeneous nucleation, with peak rates increasing stronger than exponentially with  $n_{\text{seed}}$  in the transition region. Above the transition, their crystallite density

scaled linearly with their seed density. By contrast, at the presently studied low meta-stabilities, homogeneous nucleation is practically absent. Further, a small but significant density difference exists between melt and crystal phase across coexistence (see Fig. 1(a)), our seed fractions are much larger, and our overall nucleation rate densities are still small. Thus, despite complete wetting, not every seed can actually form a crystal due to the quench in nucleation rate seen in Fig. 2a. Given such a quench,  $\eta$  could only approach unity for very small seed fractions, where the change in melt density is negligible and/or for larger nucleation rates. Only then, all seeds form their crystals before a significant change of melt properties has occurred. Consequently,  $\eta < 1$  in all present experiments. Encouraged by this finding, we replot the heterogeneous rate densities of Fig. 2(d) in Fig. 5(c) in dependence on  $n\Delta\mu$ . Now, the nucleation rate densities arrange on a single straight line. i.e. we find the nucleation rates to show the empirical relation:  $J_{\text{het}} \propto \exp(n\Delta\mu)$  in this region with seeding efficiency below unity. For future experiments, it remains to be explored, whether the strong dependency on  $n$  is retained for  $\eta \geq 1$ , or whether it switches to a linear dependency through  $n_{\text{seed}} = n f_{\text{seed}}$ .

Our observation puts a clear constraint on the range of applicability of CNT parameterization. In fact, no additional  $n$ -dependence of the exponential beyond that of  $\Delta\mu$  can be constructed within CNT including its extensions to heterogeneous nucleation. Arguably, the two main difficulties for CNT in the present case are the neglect of microscopic structure and the assumption of kinetics being based on single particle addition. Reflecting the course of theoretical and numerical research on heterogeneous nucleation, it seems that much of it was influenced by the results of the pioneering studies on hard sphere melts [35, 32, 98]. For the close packing HS systems, any impurity of size larger than average will distort local structure and hamper crystal formation due to incommensurability. Only in the limit of large radii of curvature a seed with smooth, hard surface approaches the limit of a flat hard surface. It then is wetted [99] and may serve as seed. By contrast, impurities in CS systems are readily integrated into the local structure of both melt and crystal [75]. This applies in particular for small impurities, which are of similar size as the majority species. In the heterogeneous nucleation of CS, a consideration of local microscopic structure therefore seems to be crucial for both the solid and the fluid phase. In the solid, the seed introduces a local strain field associated with an excess elastic energy. The local structure of charged sphere fluids and melts is of body centred cubic symmetry about each particle [5, 57] as reflected in the corresponding pair correlation function  $g(r)$ . This structure gets more pronounced upon reducing the salt concentration and more extended upon increasing the number density [100]. In the presence of seeds, such a

structure may be broken or enhanced, depending on seed shape and charge. We anticipate that a small seed of higher than average charge may lead to a very pronounced local structure. For the surface of the growing nuclei, however, we expect, that again a bcc structure prevails [29, 28, 63], which promotes crystal growth. The long-ranged nature of interactions should also be accounted for in the dynamics. It possibly demands considering collective relaxations rather than individual rearrangements and simple self-diffusion. The present results were obtained under well-controlled experimental boundary conditions on samples with well-characterized interactions and phase behaviour. With these experimental boundary conditions known, it appears promising to address them in simulation approaches with suitable small seeds including doublets.

Also on the experimental side, much work remains to be done. Obviously a first set of systematic experiments should address salt concentration dependent nucleation at low meta-stabilities with a preparation set-up including an online filtering. Second, our findings suggest to perform a comparison of seed-free nucleation to nucleation with seeds of same size but larger charge. Corresponding studies are under way and will be reported elsewhere. Thirdly, it seems very promising to observe heterogeneous nucleation at tweezed doublets in a confocal microscopy set up [37]. This approach would reveal valuable information about the local structure of the melt close to the seed and facilitate comparison to the overall structure at metastable conditions. Finally, our observations may also bear some relevance to nucleation in strongly polydisperse samples. Also here, larger and more highly charged particles are present, which may in principle act as “self-heterogeneous” seeds. Due to the stronger dependence of  $J$  on  $n$ , we would expect an initial accelerated increase of nucleation rates with  $\Delta\mu$  followed by a transition to a nearly constant rate density. This could be tested in experiments combining microscopy, time-resolved static light scattering, and reflection microscopy to cover an extended range of number densities.

#### **IV. CONCLUSIONS**

We here for the first time investigated the nucleation of colloidal crystals from their melt in dependence on the salt concentration. Instead of homogeneous nucleation, we observed heterogeneous nucleation at seeds comparable in size to that of the particles. We attributed this unexpected finding to the use of the continuous conditioning technique. This technique favours the formation of doublets, which then form potential seeds for heterogeneous nucleation. This resulted in a qualitatively different behaviour to that known for homogeneous nucleation of

similar systems. While our observations constrain the range of applicability of classical nucleation theory, they call for further treatment by more sophisticated approaches. In particular, investigations of seeded nucleation in CS systems with small, highly charged seeds appear to be very promising. We anticipate that the present study will motivate such research, but also additional experiments on charged sphere systems under variation of seed size and charge. The latter are highly desired to provide a comprehensive data base for the development of a deepened understanding of both homogeneous and heterogeneous nucleation in these model systems and beyond.

## **ACKNOWLEDGEMENTS**

We thank L. Shapran for contributing to the effective charge characterization, H. J. Schöpe for assistance in data evaluation and M. Evers for the composition analysis. P. Wette and D. Herlach gave valuable input in experimental issues. We are further indebted to our theoretical colleagues, with whom we had numerous interesting discussions: J. Horbach, H. Löwen, T. Schilling. Financial support of the DFG is gratefully acknowledged.

## **Conflict of Interests**

The authors declare that they have no conflict of interest.

## **Data Availability Statement**

Original data are available from the corresponding author upon reasonable request.

## APPENDIX A: ADDITIONAL DETAILS OF SYSTEM CONDITIONING AND CHARACTERIZATION

The original sample was shipped at a packing fraction of  $\Phi \approx 0.08$ . By dilution with distilled water, we prepared suspensions of approximately  $\Phi = 0.01$ , added mixed-bed ion exchange resin (IEX) [Amberlite UP 604, Rohm & Haas, France] and left it to stand with occasional stirring for some weeks. The suspension then was filtered using Millipore 0.5  $\mu\text{m}$  filters to remove dust, ion-exchange debris and coagulate regularly occurring upon first contact of suspension with IEX. A second batch of carefully cleaned IEX filled into a dialysis bag was then added to retain low ionic strength in the stock suspensions now kept under Ar atmosphere.

All further sample preparation and the measurements were performed in a closed system including the measuring cells and the preparation units [101,79]. In short, the suspension is pumped peristaltically through a closed Teflon® tubing system connecting i) the ion exchange chamber; ii) a reservoir under inert gas atmosphere to add suspension, water or salt solutions; iii) a cell for conductivity measurements and iv) one or more cells for the optical experiments. A suitable amount of stock suspension is filled under filtering into the circuit and further diluted with distilled water to the desired concentration. As this results in some particle loss, we can check the final particle density by static light scattering. By default the circuit is equipped with an online filter. Here this component was omitted to avoid further particle loss during conditioning and to work at strictly constant number density. The suspension is cycled until a stable minimum conductivity is reached, defining the deionized state. Then the ion exchange chamber is bypassed and salt solution added to adjust the electrolyte concentration under conductometric control. Care is taken to assure a leak-free circuit. This facilitates stable experimental conditions on a typical time scale of an hour, during which different measurements can be performed. In the salt concentration dependent measurements of the present work, we deionized the suspension again after each crystallization run. This avoids dilution errors in the salt concentration and accumulation of leaked carbonic acid.

For static and dynamic light scattering, as well as for Torsional Resonance Spectroscopy [102], we used quartz cells of 1cm outer diameter mounted to a multipurpose light scattering set-up described elsewhere [103]. This instrument allows measurements of the form factor of non-interacting suspensions, of the structure factor of fluid samples, and – for crystalline samples – of the particle number density from the position of Bragg reflections as well as of the shear modulus from the location of mechanical resonances in frequency space.

Conductivity [76] is measured at a frequency of  $\omega = 400$  Hz [electrodes LTA01 and LR325/01 with bridge LF538 or electrode LR325/001 with bridge LF340, WTW, Germany]. To check for reproducibility we compared conductivity values at different frequencies  $\omega \leq 1$  kHz but found no dependence on  $\omega$ . Thus  $\omega$  is low enough to measure the DC-limit of conductivity but large enough to inhibit significant electrophoretic particle transport. Care was further taken to control the suspension temperature within 1K. In general the reproducibility of conductivity measurements in suspensions was found to be better than 2%. Fig. S1 (a) shows the conductivity of PS109\* in the deionized state as a function of increased number density. We obtain a linear relation with an offset of  $\sigma_B \approx 60 \text{ nS cm}^{-1}$  due to water hydrolysis. In the deionized state, the  $n$ -dependent conductivity reads:

$$\sigma = \sigma_0 + \sigma_B = neZ_\sigma (\mu_P + \mu_{H^+}) + \sigma_B \quad (\text{A1});$$

where  $\mu_P$  and  $\mu_{H^+}$  are the electro-phoretic particle and proton mobility, respectively. The least squares fit to the data returns  $Z_\sigma = 459 \pm 20 e^-$ .

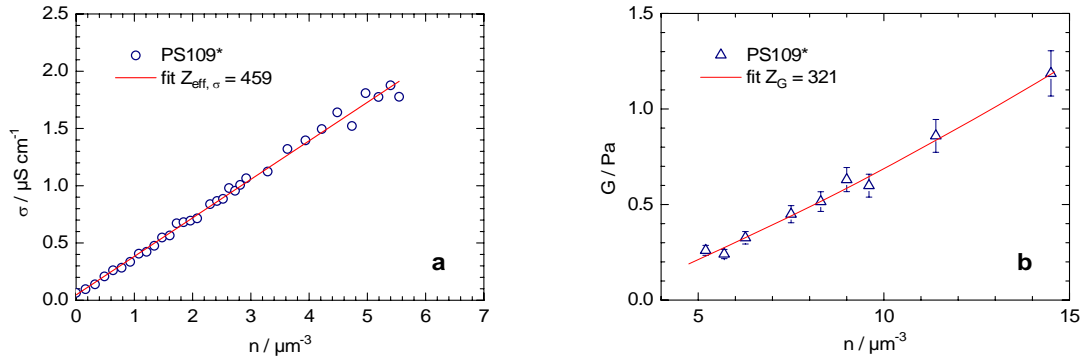


FIG A1: system characterization. (a) Sample conductivity as a function of number density. The red solid line is a least square fit of Eqn. (A1) to the data returning  $Z_\sigma = 459 \pm 20 e^-$ . (b) Sample shear modulus as a function of number density. The red solid line is a least squares fit of the Eqn. (A5) to the data returning  $Z_G = 321 \pm 18 e^-$ .

After deionization, the electrolyte concentration is adjusted by adding small amounts of NaCl solution. The exact concentration is then inferred after homogenization from the increase in conductivity using again Hessinger's model of independent ion migration.

The pair energy of interaction is modelled as a screened electrostatic repulsion neglecting van der Waals attractions. We use a mean field expression derived from the Debye-Hückel solution for ions of finite radius:

$$V(r) = \frac{Z_G^2 e^2}{4\pi\epsilon} \left( \frac{\exp(\kappa a)}{1 + \kappa a} \right)^2 \frac{\exp(-\kappa r)}{r} \quad (\text{A2}).$$

Here,  $e$  is the elementary charge, and  $\epsilon = \epsilon_0 \epsilon_r$  is the solvent dielectric permittivity. The screening parameter  $\kappa$  is defined as:

$$\kappa = \frac{e^2}{\epsilon k_B T} \sqrt{n Z_G z^2 + n_s z^2} \quad (\text{A3}),$$

where  $z = 1$  is the micro-ion valency,  $n$  is the particle number density. The micro-ion number density,  $n_s$ , is calculated accounting for ions stemming from added electrolyte and dissolved  $\text{CO}_2$  as well as ions from the self dissociation of the solvent. Note that the counter-ion density, which is explicitly accounted for through the  $nZ_{eff}$  term, contributes the majority of screening ions in our experiment.

This description assumes that individual ionic clouds overlap without distortion. Many-body effects arising from Double layer overlap are, however, accounted for by replacing  $Z_\sigma$  with  $Z_G$ . The former is determined in crystalline samples using Torsional Resonance Spectroscopy. The cylindrical sample cell containing a polycrystalline colloidal solid is put into low amplitude oscillations about its vertical axis. As the shear moduli of the sample are small, standing waves can be excited with wave lengths comparable to the container dimensions [70]. On the colloidal level, this corresponds to harmonic lattice vibrations visible as shifts of the Bragg-peaks or distortions of the first structure factor peak. These are detected and frequency analysed by time-resolved static light scattering in combination with lock-in technique. Resonance frequencies are observed at:

$$\omega_{jm}^2 = \frac{G (\mu_j^2 + (m+1)^2 \pi^2 \alpha^2)}{\rho R^2} \quad (\text{A4}),$$

where  $i$  and  $m$  are the indices of the order of the resonances,  $\alpha = 0.5$  is the ratio between the cell radius  $R$  and the filling height  $H$ ,  $\rho$  is the mass density of the suspension, and  $m_j$  are the zeros of the 1<sup>st</sup> order Bessel-function  $J_1$ .

Figure A1(b) shows the shear modulus  $G$  of deionised suspensions of PS109\* as a function of  $n$  as determined from static light scattering. It increases from  $G = 0.3\text{Pa}$  at  $n = 5\mu\text{m}^{-3}$  to  $G =$



1.2Pa at  $n = 14.5\mu\text{m}^{-3}$ . Each point represents an average over 3 to 5 measurements, the residual errors are about 5 %. The shear modulus  $G$  for crystals of bcc symmetry has been derived as [104, 105, 106]:

$$G_{bcc} = f_A \frac{4}{9} nV(d_{bcc}) \kappa^2 d_{bcc}^2 \quad (\text{A5}).$$

$f_A = 0.5$  is a numerical factor which accounts for the different boundary conditions in averaging over randomly oriented crystallites or local environs, and the nearest neighbour distance in a bcc lattice reads:

$$d_{bcc} = \frac{\sqrt{3}}{\sqrt[3]{4n}} \quad (\text{A6}).$$

Equation A6 is then used in a least squares fit to the data returning  $Z_G = 321 \pm 18e^-$ .

## APPENDIX B: CHECK FOR POTENTIAL SEED PARTICLES

We cut 4x70mm pieces from standard glass slides spin-coated with Polyvinylpyridine. When dipped into suspension, the negatively charged particles, but also dust and ion exchange debris readily adsorb. We prepared test slides from suspensions conditioned for different stretches of time. We then scanned the slides with an Atomic Force Microscope (AFM). Figure A2 shows typical a slide with no seed candidates. In fact, in most scanned areas, like in Fig. A2, none or just one candidate particle was observed, and larger objects were extremely rare. A selected example with both types of candidate seed particles is reproduced as inset of Fig. 6(a) in the main text. There, one recognizes a larger object on the upper right and two doublets in the lower part. We note that Fig. 6(a) is an exception chosen for illustration; From the average ratio of observed impurities and particles per area, we estimate an order of magnitude upper bound of impurities. For a sample conditioned for half an hour, we found a number fraction of doublets (larger objects) of  $f_D = \langle N_{\text{impurity}} / N_{\text{particle}} \rangle \leq 2 \cdot 10^{-4}$  (hardly any larger objects). After six hours of cycling we found  $f_D \leq 10^{-3}$  ( $f_L \leq 10^{-6}$ ). Interestingly, no triplets were observed. Integrating a 0.4 $\mu\text{m}$  pore size filter and cycling for one hour reduced the impurity fraction considerably to  $f_D \leq 10^{-6}$  (no larger objects), and at the same time, it reduced the num-

ber density by some 8%. From this we conclude that our doublets mainly formed already during pre-conditioning. Taking the value obtained for six hours of cycling and neglecting the splinter contribution, this amounts to a seed number density of  $n_{\text{seed}} \leq 5.4 \cdot 10^{15} \text{m}^{-3}$  and  $n_{\text{seed}} \leq 9.5 \cdot 10^{15} \text{m}^{-3}$  for the two crystallization experiments at lower and higher particle concentration, respectively.

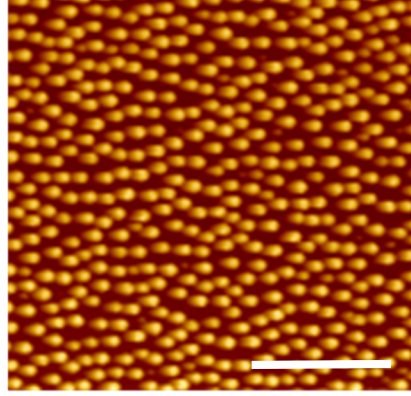


FIG A2: typical AFM image of PS109\* particles deposited on Polyvinylpyridine-coated glass slides during dip coating. Scale bar 4 $\mu\text{m}$ .

### APPENDIC C: CNT FOR COLLOIDAL SYSTEMS

CNT originally was originally designed to model condensation from the vapour phase. It was adapted to the case of crystallization in colloidal suspensions respecting their specific interactions and their diffusive dynamics [19]. Russel [107] approximated the kinetic pre-factor by an attempt frequency for diffusional relaxation:  $J_0 = nD_{\text{eff}} / \ell^2$ , where  $D_{\text{eff}}$  is an appropriate diffusion coefficient and  $\ell$  the corresponding length scale. Schöpe and Wette [43] further equated  $\ell^2$  to  $n^{-2/3}$  and considered the barrier shape *via* the Zeldovich factor:

$$J_0 = 1.55 \cdot 10^{11} \cdot n^{4/3} \sqrt{\gamma} \cdot D_S^L(n) \quad (\text{A7}).$$

The CNT expression for heterogeneous nucleation reads [108]:

$$J = J_0 f_{\text{seed}} \frac{\alpha(\phi)}{\sqrt{f(\phi)}} \exp\left(-\frac{\Delta G^*}{k_B T} f(\phi)\right), \quad (\text{A8}),$$

where  $\phi$  is the contact angle of the crystal phase on the substrate, and  $f(\phi)$  varies from 0 for  $\phi$

$= 0$  to  $1$  for  $\phi = \pi$ . The function  $\alpha(\phi)$  refers to the surface area of the daughter phase as a function of  $\phi$ . The special case of complete wetting on spherical substrates was first worked out in detail by Fletcher [35] and recently re-examined in [109]. Here,  $f(\phi, X)$  replaces  $f(\phi)$ , with  $X = R_{\text{seed}}/r$  being the ratio of seed size to nucleus size, and  $\alpha(\phi, X)/(f(\phi, X))^{1/2}$  is a factor of order unity. Note, that in that case, the work of formation of the critical nucleus is defined only if  $R_{\text{seed}} > r_{\text{crit}}$ . As  $X$  approaches unity from below, i.e. upon adsorption of a first layer of crystal phase  $f(\phi)$  drops steeply towards zero. Hence, the nucleation barrier in Eqn. (A8) vanishes.

#### APPENDIX D: ADDITIONAL DATA FROM CNT PARAMETERIZATION

This section contains additional data and intermediate results obtained during parameterization of both nucleation experiments with CNT.

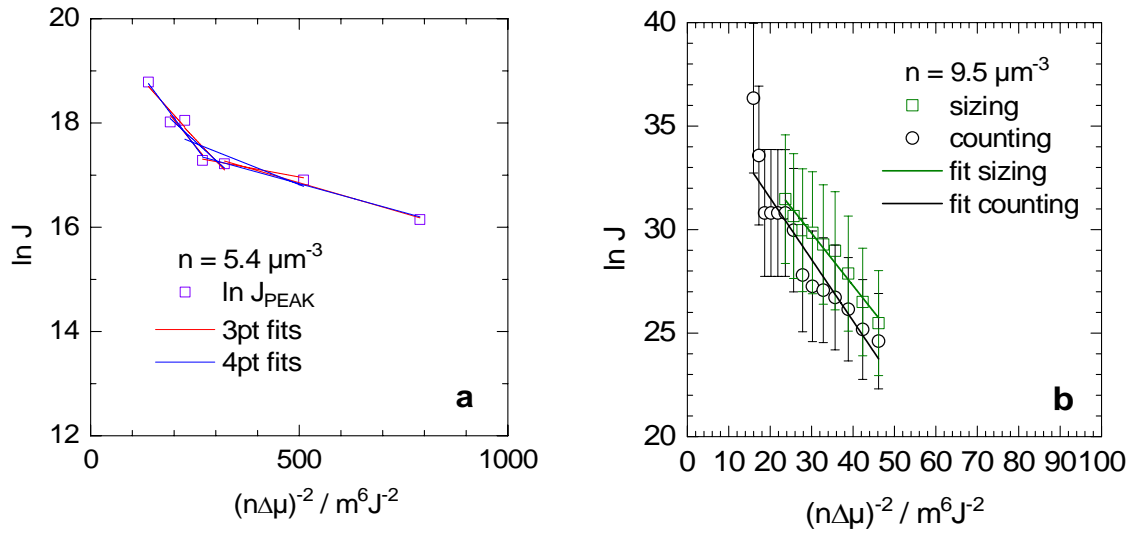


Fig. A3: CNT parameterization. (a) Natural logarithm of  $J$  plotted versus  $1/(n\Delta\mu)^2$  for the peak data obtained at  $n = 5.4\mu\text{m}^{-3}$ . Solid lines are least squares fits through three (red) and four (blue) points. (b) Natural logarithm of  $J$  plotted versus  $1/(n\Delta\mu)^2$  for the sizing (olive) and counting (black) data taken at  $n = 9.5\mu\text{m}^{-3}$ . Solid lines are least squares fits.

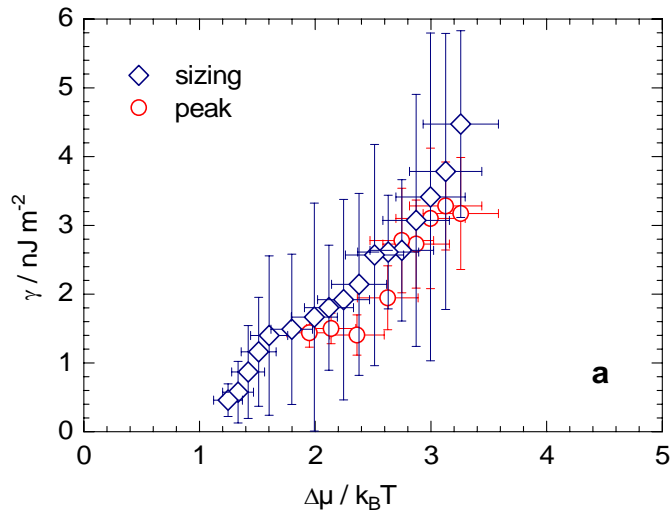


Fig. A4: Interfacial free energy as a function of metastability for the sizing and peak data obtained at  $n = 5.4 \mu\text{m}^{-3}$  as denoted by the colour code indicated in the key.

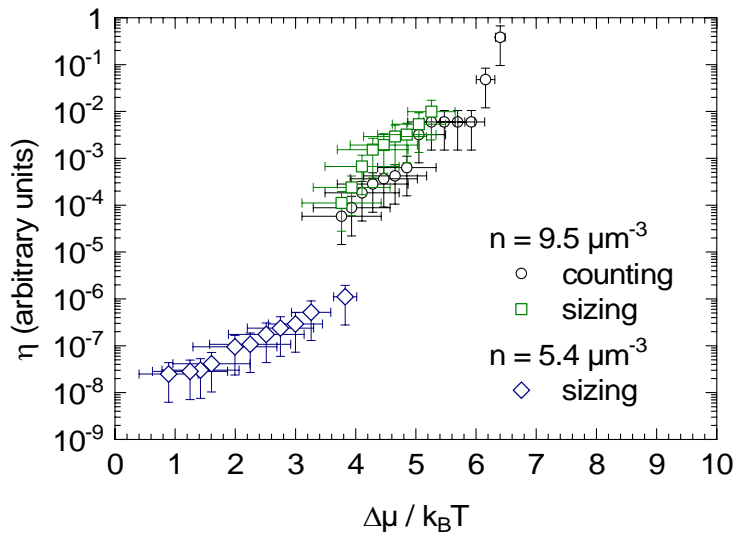


Fig. A5: Seeding efficiency calculated assuming a constant seed fraction in dependence on metastability. Data shown are for two different number densities and determined by different evaluation approaches, as indicated in the key. Note the pronounced discontinuity at  $\Delta\mu = 4k_B T$ .

## REFERENCES

---

- [1] U. Gasser, Crystallization in three- and two-dimensional colloidal suspensions, *J. Phys.: Condens. Matter* **21**, 203101 (2009).
- [2] D. M. Herlach, I. Klassen, P. Wette, D. Holland Moritz, Colloids as model systems for metals and alloys: a case study of crystallization, *J. Phys.: Condens. Matter* **22**, 153101 (2010).
- [3] H. Löwen, E. C. Oguz, L. Assoud, R. Messina, Colloidal Crystallization between two and three dimensions *Adv. Colloid Phys.* **148**, 225-249 (2012).
- [4] T. Palberg, Crystallization kinetics of colloidal model suspensions: recent achievements and new perspectives, *J. Phys.: Condens. Matter* **26**, 333101 (2014).
- [5] P. Tan, N. Xu, L. Xu, Visualizing kinetic pathways of homogeneous nucleation in colloidal crystallization, *Nature Phys.* **10**, 73–79 (2014).
- [6] J. Russo and H. Tanaka, Crystal nucleation as the ordering of multiple order parameters, *J. Chem. Phys.* **145**, 211801 (2016).
- [7] K. F. Kelton, A. F. Greer, *Nucleation in condensed Matter, Applications in Materials and Biology*, Pergamon Press, Amsterdam 2010
- [8] G. C. Sosso, J. Chen, S. J. Cox, M. Fitzner, P. Pedevilla, A. Zen, and A. Michaelides, Crystal Nucleation in Liquids: Open Questions and Future Challenges in Molecular Dynamics Simulations, *Chem. Rev.* **112**, 7078-7116 (2016).
- [9] P. Bartlett, W. v. Meegen, The Physics of Hard-Sphere Colloids, in A. Mehta (ed.), *Granular Matter* (Springer New York, 1994), 195-257.
- [10] W. C. K. Poon E. R. Weeks, C. P. Royall, On measuring colloidal volume fractions, *Soft Matter* **8** 21-30 (2012).
- [11] V. J. Anderson, H. N. W. Lekkerkerker, Insights into phase transition kinetics from colloidal science, *Nature* **416**, 811-815 (2002).
- [12] T. Zykova-Timan, J. Horbach, and K. Binder, Monte Carlo simulations of the solid-liquid transition in hard spheres and colloid-polymer mixtures, *J. Chem. Phys.* **133**, 014705 (2010).
- [13] A. Yethiraj, *Soft Matter* **3**, 1099-1115 (2007). Tunable colloids: control of colloidal phase transitions with tunable interactions
- [14] P. Wette, I. Klassen, D. Holland-Moritz, D. M. Herlach, H.J. Schöpe, N. Lorenz, H. Reiber, T. Palberg, S. V. Roth, Complete description of re-entrant phase behaviour in a charge variable colloidal model system, *J. Chem. Phys.* **132**, 131102 (2010).
- [15] H. J. Schöpe, G. Bryant, W. van Meegen, Two step crystallization kinetics in colloidal hard spheres, *Phys. Rev. Lett.* **96**, 175701 (2006).
- [16] T. Schilling, H. J. Schöpe, M. Oettel, G. Opletal, I. Snook, Precursor-mediated crystallization process in suspensions of hard spheres, *Phys. Rev. Lett.* **105**, 025701, (2010).
- [17] R. P. Sear, Non-Classical Nucleation, *Int. Mater. Rev.* **57**, 328-356 (2012).
- [18] D. Kashchiev, *Nucleation: Basic Theory with Applications*, Butterworth-Heinemann, Oxford, 2000.

- 
- [19] R. P. Sear, Nucleation: theory and applications to protein solutions and colloidal suspensions, *J. Phys.: Condens. Matter* **19**, 033101 (2007).
- [20] H. A. Wilson, On the velocity of solidification and the viscosity of supercooled liquids, *Phil. Mag.* **50**, 238-250 (1900).
- [21] J. Frenkel, Note on a relation between the speed of crystallization and viscosity, *Phys. Z. Sowjetunion* **1**, 498-500 (1932).
- [22] J. L. Harland, W. van Meegen, Crystallization kinetics of suspensions of hard colloidal spheres, *Phys. Rev. E* **55**, 3054 – 3067 (1997).
- [23] Chr. Sinn, A. Heymann, A. Stipp, T. Palberg, Solidification Kinetics in Hard Sphere Suspensions, *Prog. Colloid Polym. Sci.* **118** 266 – 275 (2001).
- [24] K. Schätzel, B. J. Ackerson, Density Fluctuations during Crystallization of Colloids, *Phys. Rev. E* **48**, 3766 (1993).
- [25] M. Franke, A. Lederer, H. J. Schöpe, Heterogeneous and homogeneous crystal nucleation in colloidal hard-sphere like microgels at low metastabilities, *Soft Matter* **7**, 11276-11274 (2011).
- [26] M. Franke, S. Golde, and H. J. Schöpe, Solidification of a colloidal hard sphere like model system approaching and crossing the glass transition, *Soft Matter* **10** 5380-5389 (2014).
- [27] W. van Meegen, T. C. Mortensen, S. R. Williams, J. Müller, Measurements of the self-intermediate scattering function of suspensions of hard spherical particles near the glass transition, *Phys. Rev. E* **58**, 6073-6085 (1998).
- [28] J. Taffs, S. R. Williams, H. Tanaka, and C. P. Royall, Structure and kinetics in the freezing of nearly hard spheres, *Soft Matter* **9**, 297-305 (2013).
- [29] B. de Nijs, S. Dussi, F. Smalenburg, J. D. Meeldijk, D. J. Groenendijk, L. Filion, A. Imhof, A. van Blaaderen, M. Dijkstra, Entropy-driven formation of large icosahedral colloidal clusters by spherical confinement, *Nat. Mater.* **14**, 56-60 (2015).
- [30] W. van Meegen, S. M. Underwood, J. Müller, T. C. Mortensen, S. I. Henderson, J. L. Harland, P. Francis, Particle diffusion and crystallization in suspensions of hard spheres, *Prog. Theor. Phys. Suppl.* **126**, 171-180 (1997).
- [31] T. Schilling, S. Dorosz, H. J. Schöpe, and G. Opletal, Crystallization in suspensions of hard spheres: a Monte Carlo and molecular dynamics simulation study, *J. Phys.: Condens. Matter* **23**, 194120 (2011).
- [32] A. Cacciuto, S. Auer, D. Frenkel, Onset of heterogeneous crystal nucleation in colloidal suspension, *Nature* **428**, 404 (2004).
- [33] K. Sandomirski, S. Walta, J. Dubbert, E. Allahyarov, A.B. Schofield, H. Löwen, W. Richtering, S.U. Egelhaaf, Heterogeneous crystallization of hard and soft spheres near flat and curved walls, *EPJ ST* **223**, 439-454 (2014).
- [34] J. R. Espinosa, C. Vega, C. Valeriani, D. Frenkel, E. Sanz, Heterogeneous versus homogeneous crystal nucleation of hard spheres, *Soft Matter* **15**, 9625-9631 (2019).
- [35] N. H. Fletcher, Size Effect in Heterogeneous Nucleation, *J. Chem. Phys.* **29** 572-576 (1958).
- [36] E. Allahyarov, K. Sandomirski, S. U. Egelhaaf, and H. Löwen, Crystallization seeds favour crystallization only during initial growth, *Nature Communications* **6**, 7110 (2015).

- 
- [37] M. Hermes, E. C. M. Vermolen, M. E. Leunissen, D. L. J. Vossen, P. D. J. van Oostrum, M. Dijkstra, and A. van Blaaderen, Nucleation of crystals on configurable seed structures, *Soft Matter* **7**, 4623-4628 (2011).
- [38] S. Auer, D. Frenkel, Prediction of absolute crystal-nucleation rate in hard-sphere colloids, *Nature* **409**, 1020 (2001).
- [39] L. Filion, M. Hermes, R. Ni, and M. Dijkstra, Crystal nucleation of hard spheres using molecular dynamics, umbrella sampling, and forward flux sampling: A comparison of simulation techniques, *J. Chem. Phys.* **133**, 244115 (2010).
- [40] M. Radu and T. Schilling, Solvent hydrodynamics speed up crystal nucleation in suspensions of hard spheres, *EPL* **105** 26001 (2014).
- [41] J. R. Espinosa, C. Vega, C. Valeriani, E. Sanz, Seeding approach to crystal nucleation, *J. Chem. Phys.* **144**, 034501 (2016).
- [42] N. Wood, J. Russo, F. Turci, C. P. Royall, Coupling of sedimentation and liquid structure: Influence on hard sphere nucleation, *J. Chem. Phys.* **149**, 204506 (2018).
- [43] P. Wette, H. J. Schöpe, Nucleation kinetics of deionized charge colloidal model suspensions: a quantitative analysis by means of classical nucleation theory, *Phys. Rev. E* **75**, 051405 (1-12) (2007).
- [44] T. Palberg, P. Wette, D. M. Herlach, Equilibrium interfacial energies and Turnbull coefficient for bcc crystallizing colloidal charged sphere suspensions, *Phys. Rev E* **93**, 022601 (2016).
- [45] H. J. Schöpe, T. Palberg, Frustration of structural fluctuations upon equilibration of shear melts, *J. Non-Cryst. Mater* **307-310**, 613-622 (2002).
- [46] P. Wette, H. J. Schöpe, T. Palberg, Crystallization in charged two component suspensions, *J. Chem. Phys.* **122**, 144901 1-8, (2005).
- [47] P. Wette, I. Klassen, D. Holland-Moritz, T. Palberg, S. V. Roth, and D. M. Herlach, Colloids as model systems for liquid undercooled metals, *Phys. Rev. E* **79**, 010501(R) (2009).
- [48] Y. Tomita, T. Seki, N. Fukaya, S. Nishikawa, N. Sato, M. Imai, M. Suko, M. Takaki, Y. Aoyama, A. Toyotama, T. Okuzono, J. Yamanaka, K. Tsukamoto, Y. Inatomi, Crystallization of Charged Colloids under Microgravity during Aircraft Parabolic Flight, *Int. J. Microgravity Sci. Appl.* **35**, 350303 (2018).
- [49] A. Stipp, R. Biehl, Th. Preis, J. Liu, A. Barreira Fontecha, H. J. Schöpe, T. Palberg, Heterogeneous nucleation of colloidal melts under the influence of shearing fields, *J. Phys. Condens. Matter* **16** S3885 – S3902 (2004).
- [50] D. J. W. Aastuen, N. A. Clark, L. K. Cotter, B. J. Ackerson, Nucleation and Growth of Colloidal Crystals, *Phys. Rev. Lett.* **57**, 1733 (1986); Erratum **57**, 2772 (1986).
- [51] J. K. G. Dhont, C. Smits, H. N. W. Lekkerkerker, A Time Resolved Static Light Scattering Study on Nucleation and Crystallization in a Colloidal Systems, *J. Colloid Interface Sci.* **152**, 386 (1992).
- [52] M. Würth, J. Schwarz, F. Culi, P. Leiderer, T. Palberg, Growth kinetics of body centred cubic colloidal crystals, *Phys. Rev. E* **52**; 6415-6423 (1995).
- [53] T. Palberg, M. R. Maaroufi, A. Stipp and H. J. Schöpe, Micro-structure evolution of wall based crystals after casting of model suspensions as obtained from Bragg microscopy, *J. Chem. Phys.* **137**, 094906 (2012).

- 
- [54] A. Engelbrecht, H. J. Schöpe, Experimental visualization of inoculation using a charged colloidal model system, *Soft Matter* **8**, 11034–11037 (2012).
- [55] H. J. Schöpe, P. Wette, Seed and wall-induced heterogeneous nucleation in charged model suspensions under microgravity, *Phys. Rev. E* **85** 051405 (2011).
- [56] P. Wette, H. J. Schöpe, T. Palberg, Microscopic investigations of homogeneous nucleation in charged sphere suspensions, *J. Chem. Phys.* **123**, 174902 (2005).
- [57] L. K. Cotter, N. A. Clark, Density fluctuation dynamics in a screened coulomb colloid: comparison of the liquid and bcc crystal phases, *J. Chem. Phys.* **86**, 6616 – 6621 (1987).
- [58] J. Liu, H. J. Schöpe, T. Palberg, An improved empirical relation to determine the particle number density in charged colloidal fluids, *Part. Part. Syst. Charact.* **17**, 206 – 212 (2000); Erratum **18** 50 (2000).
- [59] D. M. Herlach, T. Palberg, I. Klassen, S. Klein, R. Kobold, Experimental studies of crystal nucleation: metals and colloids, *J. Chem. Phys.* **145**, 211703 (2016).
- [60] C. Desgranges, J. Delhomelle, Polymorph selection during the crystallization of Yukawa systems, *J. Chem. Phys.* **126**, 054501 (2007).
- [61] S. Alexander J. P. Mc Tague, Should All Crystals Be bcc? Landau Theory of Solidification and Crystal Nucleation, *Phys. Rev Lett.* **41**, 702 (1978).
- [62] S. Xu, H. Zhou, Z. Sun, J. Zie, Formation of an fcc phase through a bcc metastable state in crystallization of charged colloidal particles, *Phys. Rev. E* **88**, 010401(R) (2010).
- [63] K. Kratzer, A. Arnold, Two-stage crystallization of charged colloids under low supersaturation conditions, *Soft Matter* **11**, 2174-2182 (2015).
- [64] D. J. W. Aastuen, N. A. Clark, J. C. Swindal, C. D. Muzny, Determination of the colloidal crystal nucleation rate density, *Phase Transitions* **21**, 139-155 (1990).
- [65] A. Engelbrecht, R. Meneses, H. J. Schöpe, Heterogeneous and homogeneous crystal nucleation in a colloidal model system of charged spheres at low metastabilities, *Soft Matter* **7**, 5685-5690 (2011).
- [66] Y. Monovoukas, A. P. Gast, The experimental phase diagram of charged colloidal suspensions *J. Colloid Interface Sci.* **128**, 533-548 (1989).
- [67] T. Palberg, W. Mönch, F. Bitzer, T. Bellini, R. Piazza, Freezing transition for colloids with adjustable charge: a test of charge renormalization, *Phys. Rev. Lett.* **74**, 4555-4558 (1995).
- [68] A. P. Gast, Y. Monovoukas, A new growth instability in colloidal crystallization, *Nature* **351**, 552-555 (1991).
- [69] T. Palberg, W. Mönch, J. Schwarz, P. Leiderer, Grain size control in polycrystalline colloidal solids, *J. Chem. Phys.* **102**, 5082-5087 (1995).
- [70] H. M. Lindsay, P. M. Chaikin, Elastic properties of colloidal crystals and glasses, *J. Chem. Phys.* **76**, 3774-3781 (1982).
- [71] W. D. Dozier, P. M. Chaikin, Periodic structures in colloidal crystals with oscillatory flow, *J. Phys. France* **43**, 843-851 (1982).
- [72] H. Löwen, R. Simon, T. Palberg, A dynamical criterion for the freezing of Brownian particles, *Phys. Rev. Lett.* **70**, 1557-1561 (1993).
- [73] R. Simon, T. Palberg, P. Leiderer, Structurally determined Brownian dynamics of ordered colloidal suspensions, *J. Chem. Phys.* **99**, 3030-3036 (1993).



- 
- [74] T. Palberg, M. Würth, Multiphase coexistence and non-linear rheology of colloidal suspensions in an optical model capillary viscosimeter, *J. Phys I (France)* **6**; 237-244 (1996).
- [75] N. J. Lorenz, H. J. Schöpe, H. Reiber, T. Palberg, P. Wette, I. Klassen, D. Holland-Moritz, D. Herlach and T. Okubo, Phase behaviour of deionized binary mixtures of charged colloidal spheres, *J. Phys.: Condens. Matter* **21**, 464116 (2009).
- [76] D. Hessinger, M. Evers, T. Palberg, Independent Ion Migration in Suspensions of Strongly Interacting Charged Colloidal Spheres, *Phys. Rev. E* **61**, 5493 - 5506 (2000).
- [77] M. Medebach, R. Chuliá Jordán, H. Reiber, H.-J. Schöpe, R. Biehl, M. Evers, D. Hessinger, J. Olah, T. Palberg, E. Schönberger, P. Wette, Drude like conductivity in charged sphere colloidal crystals: density and temperature dependence, *J. Chem. Phys.* **123**, 104903 (2005).
- [78] T. Palberg, H. Hecht, E. Simnacher, T. Loga, F. Falcoz, J. Kottal, P. Leiderer, Determination of the shear modulus of colloidal solids with high accuracy, *J. Phys. III (France)* **4**, 457-471 (1994).
- [79] P. Wette, H.-J. Schöpe, R. Biehl, T. Palberg, Conductivity of deionised two-component colloidal suspensions, *J. Chem. Phys.* **114**, 7556 - 7562 (2001).
- [80] R. Higler, J. Sprakel, Doping colloidal bcc crystals - interstitial solids and meta-stable clusters, *Sci. Rep.* **7**, 12634 (2017).
- [81] M. N. van der Linden, A. van Blaaderen, and M. Dijkstra, Effect of size polydispersity on the crystal-fluid and crystal-glass transition in hard-core repulsive Yukawa systems, *J. Chem. Phys.* **138**, 114903 (2013).
- [82] M. O. Robbins, K. Kremer, and G. S. Grest, Phase diagram and dynamics of Yukawa Systems, *J. Chem. Phys.* **88**, 3286-3312 (1988).
- [83] T. Palberg, Crystallisation kinetics of repulsive colloidal spheres, *J. Phys.: Condens. Matter* **11**, R323 - R360 (1999).
- [84] M. Avrami, Kinetics of Phase Change. I: General Theory, *J. Chem. Phys.* **7**, 1003 (1939); Kinetics of Phase Change. II: Transformation-Time relations for random distribution of nuclei, **8**, 212 (1940); Kinetics of Phase Change. III: Granulation, Phase Change and Microstructures, **9**, 177 (1941).
- [85] C. W. Van Sice, Random nucleation and growth kinetics, *Phys. Rev. B* **54**, 11845 (1996).
- [86] W. A. Johnson, R. F. Mehl, Reaction kinetics in processes of nucleation and growth, *Trans. A. I. M. M. E.* **135**, 416 - 458 (1939).
- [87] K. F. Kelton, Crystal nucleation in liquids and glasses, *Solid State Physics* **45**, 75-177 (1991).
- [88] R. Becker, W. Döring, Kinetische Behandlung der Keimbildung in übersättigten Dämpfen, *Ann. Phys.* **24**, 719-752 (1935).
- [89] J. Zeldovich, A theory of the ignition on incandescent surfaces, *J. Exptl. Theoret. Phys. (U.S.S.R.)* **12**, 525 (1942).
- [90] J. Frenkel, *Kinetic Theory of Liquids* (Oxford University Press, New York, 1946).
- [91] D. Turnbull, J. C. Fisher, Rate of nucleation in condensed systems, *J. Chem. Phys.* **17**, 71 (1949).
- [92] J. H. Hollomon, D. Turnbull, Nucleation, *Prog. Metal Phys.* **4**, 333-388 (1953).

- 
- [93] D. Kashchiev, Solution of the non-steady state problem in nucleation kinetics, *Surf. Sci.* **14**, 209-220 (1969).
- [94] J. Bokeloh, G. Wilde, R.E. Rozas, R. Benjamin, J. Horbach, Nucleation barriers for the liquid-to-crystal transition in simple metals: Experiment vs. simulation, *EPJ ST* **223** 511-526 (2014).
- [95] D. Kashchiev, Toward a better description of the nucleation rate of crystals and crystalline monolayers, *J. Chem. Phys.* **129**, 164701 (2008).
- [96] G. Nägele, M. Kollmann, R. Pesche, A. J. Banchio, Dynamic properties, scaling and related freezing criteria of two- and three-dimensional colloidal dispersions, *Mol. Phys.* **100.**, 2921-2933 (2002).
- [97] A. Engelbrecht, H. J. Schöpe, Drastic Variation of the Microstructure Formation in a Charged Sphere Colloidal Model System by Adding Merely Tiny Amounts of Larger Particles, *Crystal Growth and Design* **10**, 2258 – 2266 (2010).
- [98] S. Auer, D. Frenkel, Suppression of crystal nucleation in polydisperse colloids due to increase of the surface free energy, *Nature* **413**, 711 (2001).
- [99] M. Dijkstra, Capillary freezing or complete wetting of hard spheres in a planar slit, *Phys. Rev. Lett.* **93**, 108303 (2004).
- [100] J. Gapinski, A. Wilk, A. Patkowski, W. Häußler, A. J. Banchio, R. Pecora, G. Nägele, Diffusion and microstructural properties of solutions of charged nanosized proteins: Experiment versus theory, *J. Chem. Phys.* **123**, 054708 (2006).
- [101] T. Palberg, W. Härtl, U. Wittig, H. Versmold, M. Würth, E. Simnacher, Continuous deionization of latex suspensions, *J. Phys. Chem.* **96**, 8180-8183 (1992).
- [102] P. Wette, H. J. Schöpe, T. Palberg, Comparison of colloidal effective charges from different experiments, *J. Chem. Phys.* **116**, 10981-10988 (2002).
- [103] H.-J. Schöpe, T. Palberg, A multipurpose instrument to measure the vitreous properties of charged colloidal solids, *J. Colloid Interface Sci.* **234**, 149-161 (2001).
- [104] Encyclopedia of Physics Vol.VII, Part I, “*Crystal Physics I*” Springer, Berlin, 1955.
- [105] R. A. Johnson, Relationship between Two-Body Interatomic Potentials in a Lattice Model and Elastic Constants, *Phys. Rev. B* **6**, 2094 (1972).
- [106] J. F. Joanny, Acoustic shear waves in colloidal crystals, *J. Colloid and Interface Sci.*, **71**, 622 (1979).
- [107] W. B. Russel, On the dynamics of the disorder-order transition, *Phase Transitions* **21**, 127 (1990).
- [108] K. F. Kelton, A. F. Greer, *Nucleation in condensed Matter, Applications in Materials and Biology*, Pergamon Press, Amsterdam 2010.
- [109] H. Vehkamäki, A. Määttänen, A. Lauri, I. Napari, M. Kulmala, Technical note: The heterogeneous Zeldovich factor, *Atmos. Chem. Phys. Discuss.* **6**, 9069–9083 (2006).